



## Article

# Study on the Optimal Double-Layer Electrode for a Non-Aqueous Vanadium-Iron Redox Flow Battery Using a Machine Learning Model Coupled with Genetic Algorithm

Qiang Ma <sup>1,2</sup> , Wenxuan Fu <sup>2</sup>, Jinhua Xu <sup>3</sup>, Zhiqiang Wang <sup>1,\*</sup> and Qian Xu <sup>2,\*</sup> 

<sup>1</sup> School of Mechanical and Vehicle Engineering, Nanchang Institute of Science and Technology, 998 Gezaoshan Road, Nanchang 330108, China; maqiang@ujs.edu.cn

<sup>2</sup> Institute for Energy Research, Jiangsu University, 301 Xuefu Road, Zhenjiang 212013, China; xuan06210621@126.com

<sup>3</sup> School of Advanced Manufacturing, Nanchang University, Nanchang 330031, China; kingward\_xjh@126.com

\* Correspondence: zqwang89@163.com (Z.W.); xuqian@ujs.edu.cn (Q.X.)

**Abstract:** To boost the operational performance of a non-aqueous DES electrolyte-based vanadium-iron redox flow battery (RFB), our previous work proposed a double-layer porous electrode spliced by carbon paper and graphite felt. However, this electrode's architecture still needs to be further optimized under different operational conditions. Hence, this paper proposes a multi-layer artificial neural network (ANN) model to predict the relationship between vanadium-iron RFB's performance and double-layer electrode structural characteristics. A training dataset of ANN is generated by three-dimensional finite-element numerical simulations of the galvanostatic discharging process. In addition, a genetic algorithm (GA) is coupled to an ANN regression training process for optimizing the model parameters to elevate the accuracy of ANN prediction. The novelty of this work lies in this modified optimal method of a double-layer electrode for non-aqueous RFB driven by a machine learning (ML) model coupled with GA. The comparative result shows that the ML model reaches a satisfactory predictive accuracy, and the mean square error of this model is lower than other popular ML regression models. Based on the known region of operating conditions, the obtained results prove that this well-trained ML algorithm can be used to estimate whether a double-layer electrode should be applied to a non-aqueous vanadium-iron RFB and determine an appropriate thickness ratio for this double-layer electrode.

**Keywords:** machine learning; artificial neural network; genetic algorithm; redox flow battery; gradient porous electrode; operational performance; DES electrolyte; 3D finite-element numerical simulation; vanadium-iron



**Citation:** Ma, Q.; Fu, W.; Xu, J.; Wang, Z.; Xu, Q. Study on the Optimal Double-Layer Electrode for a Non-Aqueous Vanadium-Iron Redox Flow Battery Using a Machine Learning Model Coupled with Genetic Algorithm. *Processes* **2023**, *11*, 1529. <https://doi.org/10.3390/pr11051529>

Academic Editor: Antonio Bertei

Received: 9 April 2023

Revised: 9 May 2023

Accepted: 13 May 2023

Published: 17 May 2023



**Copyright:** © 2023 by the authors. Licensee MDPI, Basel, Switzerland. This article is an open access article distributed under the terms and conditions of the Creative Commons Attribution (CC BY) license (<https://creativecommons.org/licenses/by/4.0/>).

## 1. Introduction

Renewable energy generation technology is replacing traditional fossil fuels partly to meet the global targets for carbon peaking and carbon neutrality. However, to address the grid destabilization caused by the intermittent nature of renewable energy, it still needs to develop appropriate energy storage technology to store or release power produced by grid-connected renewable sources [1]. Therein, as an electrochemical energy storage and conversion device, redox flow batteries (RFBs) have shown their particular advantages in the grid-scale energy storage system due to their flexible design of energy storage and power components, long charging/discharging cycle life and environmental friendliness [2]. Although an all-vanadium redox flow battery (VRFB) with an aqueous electrolyte has been applied in commercial energy storage engineering, the low energy density (ca. 15–25 Wh/L) [3] of the VRFB also limits its applied range. To further boost the energy storage density of RFB's electrolyte, non-aqueous solvents were proposed to be applied in RFBs, due to the used non-aqueous solvents having the broader voltage window

width and the higher species solubility, thus improving the theoretical energy storage density of RFB [4–6]. For the past few years, non-aqueous deep eutectic solvents (DESs), which are typical non-aqueous solvents, have been applied in several RFB systems [7]. The existing report [8] shows that the hydroquinone (H2BQ)-based RFB using a DES catholyte has an energy density of 114 Wh/L, and the energy density of aluminum-based RFB with DES can reach 189 Wh/L, which is 7.5 times that of VRFB. Nevertheless, high-viscosity DES would lead to large hydraulic resistance, and poor reaction kinetics activity also limits the energy efficiency and power density of DES electrolyte-based RFBs.

A porous carbon electrode is the core unit of an RFB device. Porous electrode architectures determine the electrolyte momentum transfer and ion mass transfer behaviors. The surface of the carbon electrode provides the active sites for electrochemical reactions. As a result, a desired electrode, including low transfer resistance, large reactive specific surface area, and high electrochemical reversibility [9–11], would substantially improve the performance of RFBs with an aqueous or non-aqueous electrolyte. During the charging/discharging operation process, the electrolyte flow rate, the ions mole concentration, and the reactive charge density have typical heterogeneous distribution characteristics inside the porous electrode structure. Moreover, there often exists a contradiction between reducing flow resistance and increasing reactive active sites for the design of electrodes. In order to improve the synergistic efficiencies of nonuniform coupled transfer and electrochemical reaction, gradient electrode architectures [12–15] were proposed to regulate the distribution uniformity of coupled transfer and electrochemical reaction [16] and make a trade-off between the transfer resistance loss and the reactive polarization loss at different sites within the electrode [17]. Recently, we reported a double-layer porous electrode spliced by carbon paper (CP), and graphite felt (GF) for a DES electrolyte-based vanadium-iron RFB [18]. Utilizing the thermal oxidation method that can decrease the activation polarization loss and improve the hydrophilicity of carbon electrodes (including CP and GF) [19], this composite electrode with a low-porosity CP electrode treated by thermal oxidation is assembled near the membrane side, which is adopted to promote the reaction kinetics and flow hydrophilicity in this region with high overpotential and low fluidity. Meanwhile, a high-porosity GF electrode deposited on copper nanoparticles is assembled near the flow field side as a supporting layer. This is expected to reduce the flow/ions/charge transfer resistance simultaneously. The experimental study shows that the peak power density of this double-layer porous electrode is 30.2% higher than that of a pristine GF electrode. Nonetheless, to guide the design of gradient/multi-layer electrode architectures (e.g., porosity distribution of gradient electrode, the thickness ratio of CP to GF of double-layer electrode), it is necessary to develop an accurate predictive model to reveal the relationship between the RFB's performance and porous electrode structural characteristics.

Compared with the high economic cost and time-consuming experimental study, numerical simulation methods have become powerful tools for investigating the coupled transfer and electrochemical reaction behaviors of batteries [20]. However, considering the massive amount of operational conditions of an RFB and diverse gradient electrode architectures, numerical models cannot quickly screen a bulk of electrode architectures to address RFB design problems under the entire operational condition range [21]. Conversely, machine learning (ML) algorithms have been successfully applied to analyze the influence laws of performance for different battery types based on limited experimental or numerical cases as training data [22–24]. As a classic ML algorithm, it has been proved that the artificial neural network (ANN) algorithm could task the regression prediction of battery performance affected by the electrode structures efficiently and accurately [20,21,25]. However, the related published research lacked a reasonable ANN model to aid the optimal design of double-layer electrode architectures for non-aqueous RFBs.

Here, this paper proposes a multi-layer ANN coupled with a genetic algorithm (GA) to optimize the double-layer gradient electrode architectures for reducing the total power loss of a DES electrolyte-based vanadium-iron RFB during galvanostatic discharging. The training dataset of the ML algorithm is generated by three-dimensional finite-element nu-

merical simulations. This validated, well-trained ML model can give the optimal thickness ratio of the double-layer electrode during the galvanostatic discharging of an RFB under different operational conditions.

## 2. Methods

### 2.1. Scheme of Machine Learning Model Coupled with Genetic Algorithm

Figure 1 illustrates this framework of ANN coupled with a genetic algorithm to optimize double-layer gradient electrode architectures. Firstly, a three-dimensional finite-element numerical model was established to simulate the operation performance of vanadium-iron RFB and generate a training dataset for ML applications. Then, a multi-layer ANN coupled with GA was used to carry out the regression training based on the acquired dataset, thus predicting the effects of RFB's operating conditions and electrode architectural features on its performance represented by total power loss. Finally, combined with a well-trained prediction model, this study aims to clarify the optimized ratio of CP thickness to total electrode thickness under the different operating conditions of a DES electrolyte-based vanadium-iron RFB.

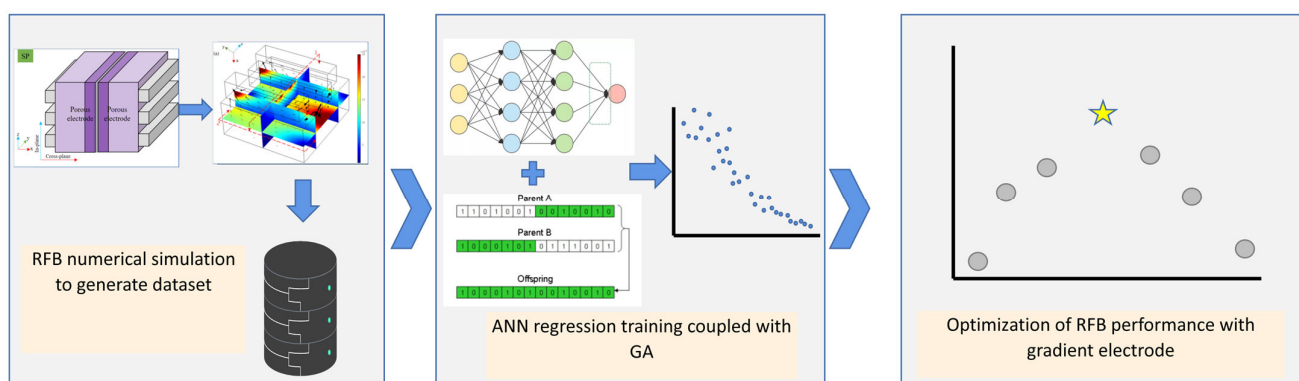
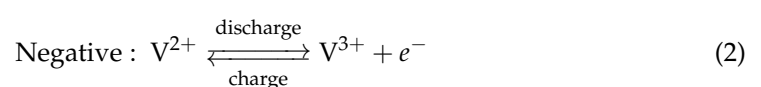
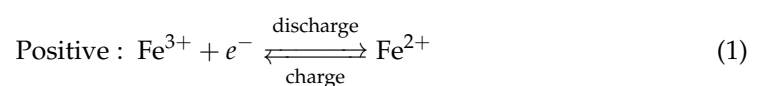


**Figure 1.** Framework of ANN coupled with genetic algorithm.

### 2.2. 3D Numerical Model of DES Electrolyte-Based Vanadium-Iron RFB

In our previous reports [26–30], we have tried to clarify the REV-scale and pore-scale reactive transfer behaviors of a DES electrolyte-based vanadium-iron RFB and revealed the influence laws of electrode architectures on this RFB's performance. Based on these works, we established a 3D single-cell geometric model of vanadium-iron RFB, which includes the double-layer composite porous electrode, as shown in Figure 2a. It can be found that the GF electrode is assembled near the flow channel side, and the CP electrode is assembled near the membrane side. Notably, the thickness ratio of CP to GF is variable in this study, thereby seeking an optimized composite electrode architecture. The galvanostatic discharge of this DES electrolyte-based vanadium-iron RFB with different operating conditions and thickness ratios is simulated by the finite-element computing platform, i.e., the COMSOL Multiphysics® package. The electrochemical reactions occurring in positive and negative electrodes are described as follows:



The detailed computing method, mesh generation and validation mode are described in our published literature [29,30]. Moreover, a fixed state of charge (SOC, SOC = 0.5) is employed at the inlet of the flow channel during these simulations; the detailed boundary conditions and geometric dimensioning of this model are listed in Tables 1 and 2, respec-

tively. As the flow flux of 25 mL/min is chosen, Figure 2b plots the polarization curve of the mono-layer CP electrode simulated by this FEM model and the numerical result of the validation model with previous experimental data [29]. It can be observed that the average relative error is 3.3%, which demonstrates the accuracy of the present model.

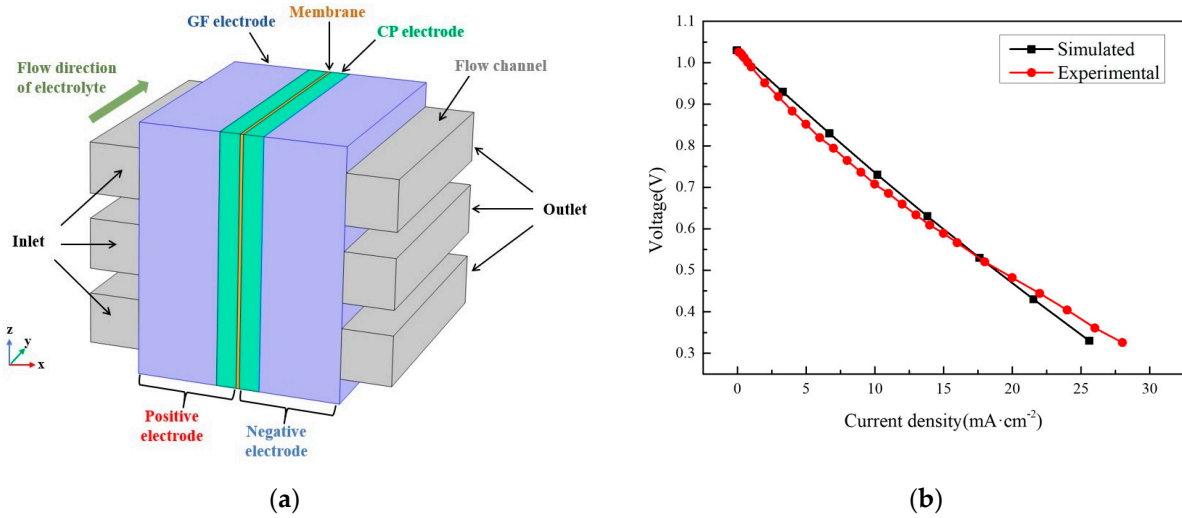


Figure 2. (a) Schematic of a numerical model of RFB, (b) Verification case.

Table 1. Boundary conditions of this work.

Types	Boundaries	Descriptive Equations
Charge transfer boundary	Galvanostatic boundary on the positive side Ground boundary on the negative side Insulation boundary for other walls	$-\sigma_s^{eff} \nabla \varphi_s \cdot \mathbf{n} = -I$ $\varphi_s = 0$ $-\mathbf{n} \cdot \mathbf{i}_l = 0, -\mathbf{n} \cdot \mathbf{i}_s = 0$
Momentum transfer boundary	Constant electrolyte flow rate boundary at the inlet Constant pressure boundary at the outlet Non-slip flow condition for other boundaries	$v_{in} = \frac{Q}{\varepsilon \cdot A}$ $P_{out} = 0$ $\nabla p \cdot \mathbf{n} = 0$
Mass transfer boundary	Constant SOC boundary at the inlet Full development boundary at the outlet Non-permeate boundary for other walls	$c_{V(II)_{in}} = c_{0\_neg} \cdot SOC$ $c_{V(III)_{in}} = c_{0\_neg} \cdot (1 - SOC)$ $c_{Fe(II)_{in}} = c_{0\_pos} \cdot (1 - SOC)$ $c_{Fe(III)_{in}} = c_{0\_pos} \cdot SOC$ $c_{Cl\_neg} = 2c_{0\_neg} \cdot SOC + 3c_{0\_neg} \cdot (1 - SOC)$ $c_{Cl\_pos} = 2c_{0\_pos} \cdot (1 - SOC) + 3c_{0\_pos} \cdot SOC$ $-D_i^{eff} \nabla c_i \cdot \mathbf{n} = 0$ $(-D_i^{eff} \nabla c_i - Z_i \mu_i^{eff} F c_i \nabla \varphi_l + c_i \mathbf{u}) \cdot \mathbf{n} = 0$

Table 2. Geometric dimensioning of the numerical model.

Geometric Parameters	Value	Unit
Cell height	10	mm
Cell width	10	mm
Total electrode thickness	4	mm
Membrane thickness	0.12	mm
Channel height	2	mm
Channel width	2	mm
Channel length	10	mm

### 2.3. Dataset Generation

In order to provide a series of appropriate training and test data for the ML model coupled with GA, we used the above finite-element numerical model to simulate the steady galvanostatic discharging process under different operating conditions and the electrode architectural features and obtain the overpotential polarization loss and pump power loss of the DES electrolyte-based vanadium-iron RFB. On the one hand, the different electrolyte flow rates and galvanostatic discharging current densities are investigated as the key factors impacting the RFB's performance. Based on our previous experimental and numerical works [18,26,29], it can be found that the studied electrolyte flow rate ( $Q$ ) mainly focuses on the range of 1–25 mL/min. Therefore, several discrete flow rates (i.e.,  $Q = 1$  mL/min, 2 mL/min, 5 mL/min, 10 mL/min, 15 mL/min, 20 mL/min, 25 mL/min) are selected input conditions. On the other hand, considering that this conventional DES-based vanadium-iron RFB often has a lower peak current density (about 200 A/m<sup>2</sup>) [31] and the overlarge reactive current density may reduce the convergence of numerical computation, the discharging current density ( $J$ ) ranging from 5 A/m<sup>2</sup> to 140 A/m<sup>2</sup> is studied in this work. The detailed discharging current densities are selected as  $J = 5$  A/m<sup>2</sup>, 10 A/m<sup>2</sup>, 20 A/m<sup>2</sup>, 30 A/m<sup>2</sup>, . . . , 140 A/m<sup>2</sup>. In addition, due to the double-layer electrode being composited by a CP and a GF electrode, the ratio of CP thickness to total electrode thickness ( $R_t$ ) is considered an adjustable variable to seek the optimized composite electrode structure. This study explores six different thickness ratios, i.e.,  $R_t = 0, 0.25, 0.375, 0.5, 0.75$  and 1. Therein,  $R_t = 0$  or  $R_t = 1$  means the composite electrode would turn into a mono-layer GF or CP electrode, respectively. Likewise,  $R_t = 0.5$  means CP thickness is equal to GF thickness for the double-layer composite electrode. By altering these input variables ( $Q, J$  and  $R_t$ ), 620 numerical simulation cases were performed to reveal the discharging performance of the DES electrolyte-based vanadium-iron RFB affected by these input variables. To simplify the complexity of this optimization problem, we used a total power loss ( $P_{total}$ ) to evaluate the overall performance of RFB, which means RFB can achieve an optimal running condition and an electrode architecture as the total power loss is minimized. In detail, the total power loss ( $P_{total}$ ) is the sum of overpotential polarization loss ( $P_{power}$ ) and pump power loss ( $P_{pump}$ ), which can be defined as

$$P_{pump} = \frac{\Delta p_{total} \cdot Q}{\eta_p} \quad (3)$$

$$P_{power} = (V_{ideal} - V_{cell}) \cdot J \cdot S \quad (4)$$

$$P_{total} = P_{pump} + P_{power} \quad (5)$$

where  $\Delta p_{total}$  stands for the total pressure drop in the positive and negative electrodes.  $Q$  and  $\eta_p$  are inlet electrolyte flow rate and pump efficiency, respectively.  $V_{ideal}$  and  $V_{cell}$  are the ideal and actual output voltage, respectively.  $V_{ideal}$  can be obtained by the difference of ideal potential between the positive and negative sides, and  $S$  is the area of the electrode. As the single output target, the total power loss calculated based on the results of 620 numerical simulation cases would be integrated with the above three input variables to generate the dataset. During the ML procedure, 75% of data (i.e., 465 cases) are randomly selected to train the ANN model and perform cross-validation, and others (i.e., 155 cases) are used to test the accuracy of the model.

### 2.4. Artificial Neural Network Model Coupled with Genetic Algorithm

ANN is a frequently-used ML algorithm to solve larger-scale problems in complex systems [22]. In this paper, a multi-layer ANN regression model was established to predict the hidden relationship between input variables and output targets that are generated from the above dataset. This ANN model contains an input layer with three nodes (i.e.,  $Q, J$  and  $R_t$ ), an output layer with one node (i.e.,  $P_{total}$ ), and two hidden layers between

them. Meanwhile, the first and second hidden layers have five and four nodes, respectively. The nodes between adjacent layers are linked by an activation function from the input node of the previous layer to the receiving node of the next layer, which includes an associated weight and a threshold. The determination process of these weights and thresholds plays a key role in the prediction accuracy of the ANN regression model. Generally, these parameters of ANN would iteratively search for the appropriate values to keep the predictive output in accord with the practical output of training data as far as possible. For the sake of improving the accuracy of the ANN model, we introduced GA to assist the ANN training process. GA is a noted stochastic search optimization method that simulates nature's genetic evolution mechanism. Compared to other metaheuristic techniques, such as simulated annealing or particle swarm optimization, GA has several advantages, including the ability to handle a large search space, high convergence rate and flexibility [32]. Overall, the advantages of genetic algorithms make them a popular choice for a wide range of optimization problems, particularly those with complex constraints or large search spaces. During this iterative process of GA, the candidate parameters (e.g., weight and threshold) that need to be optimized are coded as a tandem array named a gene. A series of stochastic coding genes would form a population. Mimicking biological evolution, some genes in this population are renewed using random selection, crossover and mutation operations to alter the coding for a portion of genes in the population. After the evolution procedure, a one-fold method is employed to perform cross-validation, thus calculating and sorting the fitness of genes, which is defined as the predictive error of ANN in this paper. Then, the gene with the lowest fitness will be replaced by the highest fitness, thus generating a new population to perform the next iteration. Using a specific population size and sufficient iterations, the highest population fitness can be improved gradually, thereby optimizing the weight and threshold to meet the expected criterion of ANN prediction accuracy. In detail, this coupled ML flow path is illustrated in Figure 3.

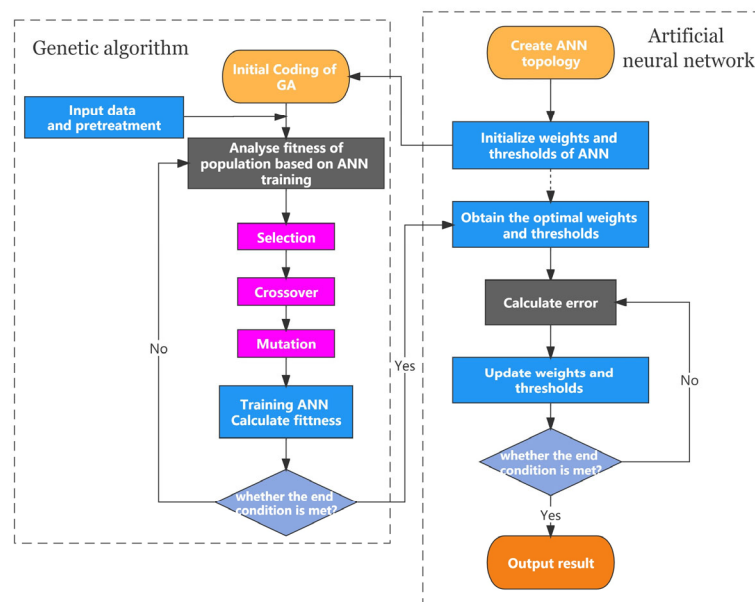


**Figure 3.** Schematic of ANN model coupled with GA.

### 3. Results and Discussions

#### 3.1. Numerical Results of RFB's Galvanostatic Discharge Process

We conducted numerical cases to simulate the galvanostatic discharge process of a vanadium-iron RFB with double-layer electrodes. In addition to generating datasets, these finite element simulations can also directly reveal the reactive transfer behaviors in porous electrodes. Figure 4 plots the  $\text{Fe}^{2+}$  ions concentration distributions of the positive electrode with different architectures during the galvanostatic discharge process. This is

done with a current density of  $70 \text{ A/m}^2$  and an electrolyte flow rate of  $2 \text{ mL/min}$ . On the one hand, compared with the mono-layer GF electrode, as shown in Figure 4b, Figure 4a plots that the double-layer electrode can provide a more sufficient specific surface area near the membrane side, which is beneficial to reduce the charge transfer current per unit area occurring near the membrane side, and improve the electrochemical reaction efficiency inside this region. On the other hand, due to the uneven porosity distribution of the double-layer electrode, the flow of electrolyte would encounter greater resistance inside the CP section with the lower porosity, leading to lower electrolyte flow near the membrane side. The above two reasons result in the reactive product concentration (i.e.,  $\text{Fe}^{2+}$  ions concentration) near the membrane side of the double-layer electrode being higher than that of the GF electrode. The numerical results reveal that the composite electrode architecture would significantly change the electrochemical reaction and coupled transfer characteristics. This would further influence the operation performance of the RFB.

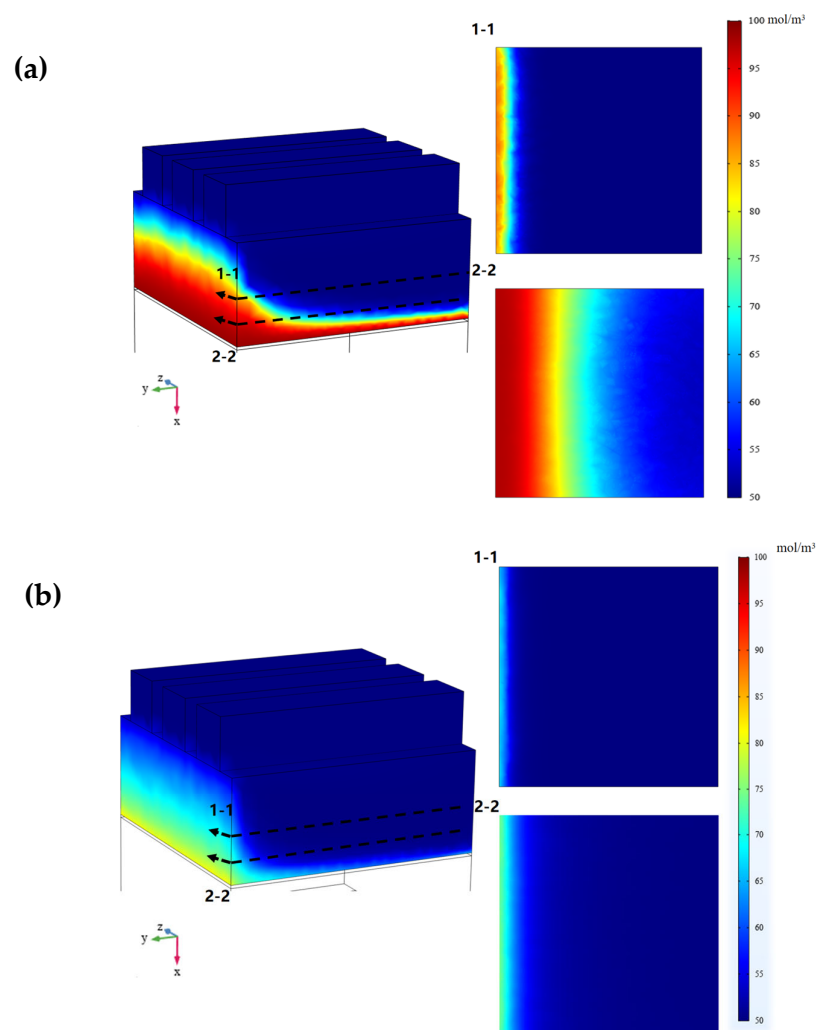


**Figure 4.**  $\text{Fe}^{2+}$  ions concentration distributions: (a) double-layer electrode ( $R_t = 0.5$ ), (b) mono-layer GF electrode ( $R_t = 0$ ).

The overpotential polarization loss derived from the numerical result is explicitly inversely proportional to the RFB's discharging efficiency. Figure 5a–c plots this overpotential polarization loss under different electrolyte flow rates and electrode architectures. For all electrode architectures, polarization losses rise observably with the increase in discharging current density. This means RFB exhibits poorer voltage efficiency under higher current density operation conditions [33]. Moreover, as shown in Figure 5, compared with GF ( $R_t = 0$ ) and CP ( $R_t = 1.0$ ) electrodes, the designed double-layer electrode ( $R_t = 0.5$ ) has a

lower polarization loss, especially for the higher flow rate and current density conditions. This result demonstrates that the composite electrode architecture can achieve higher discharging efficiency. The reason is mainly caused by the CP section near the membrane side having a larger specific surface area, thus providing a more sufficient reaction site to reduce electrochemical reaction resistance. Meanwhile, the higher porosity GF section near the flow field side can effectively diffuse the electrolyte flowing toward the CP section. The lower flow resistance loss within the GF section enhances the ion transfer to decrease the concentration polarization overpotential. However, the standalone polarization overpotential cannot reflect the overall performance of the RFB. The flow inside the porous electrode would generate an obvious Darcy flow resistance loss (i.e., pump power loss) governed by electrode architecture and electrolyte flow rate. Consequently, Figure 6a–c plots the total power loss affected by RFB operating conditions and electrode architectures. With the smaller electrolyte flow rate condition (i.e.,  $Q = 1\text{--}2\text{ mL/min}$ ), an RFB with the mono-layer GF electrode can achieve the optimum performance as the lower current density (i.e.,  $J < 20\text{ mA/m}^2$  for  $Q = 1\text{ mL/min}$  and  $J < 35\text{ mA/m}^2$  for  $Q = 2\text{ mL/min}$ ). This phenomenon is attributed to the low flow resistance of GF that reduces the pump power loss, and the polarization loss only makes up a small part of the total loss under a small current density condition. However, GF's disadvantage leads to RFB's higher polarization loss, and this impact becomes more noticeable under the larger discharging current density condition. Meanwhile, the double-layer electrode exhibits the synergistic optimization of hydraulic transfer and electrochemical reaction process. Therefore, the  $P_{total}$  of the double-layer composite electrode is less than that of the GF electrode as the suitable operation condition (i.e.,  $J > 20\text{ mA/m}^2$  for  $Q = 1\text{ mL/min}$  and  $J > 35\text{ mA/m}^2$  for  $Q = 2\text{ mL/min}$ ). On the contrary, with the higher flow rate ( $Q = 10\text{ mL/min}$ ), the pump power loss dominates the RFB's operating performance. Under this flow condition, the high porosity GF has the advantage of low hydraulic transfer resistance. Thus the double-layer electrode cannot acquire the lowest total power loss during the galvanostatic discharge process as  $Q = 10\text{ mL/min}$ . These results illustrate that the vanadium-iron RFB with a double-layer electrode only achieves the effect of optimization under limited operating conditions. Hence, it is necessary to reveal the regression relationship between the RFB's performance and the electrode architectures under the different operating conditions driven by the ML model.

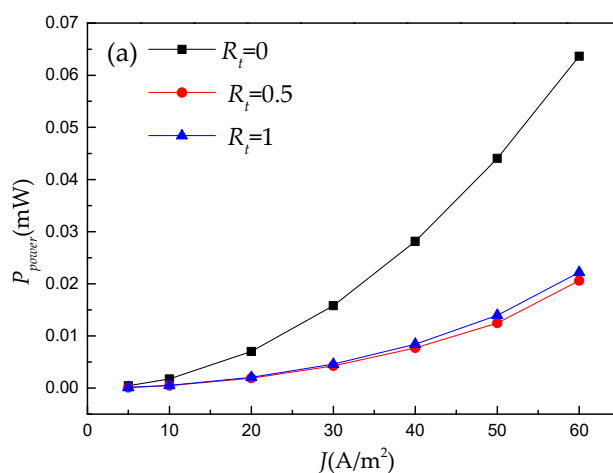
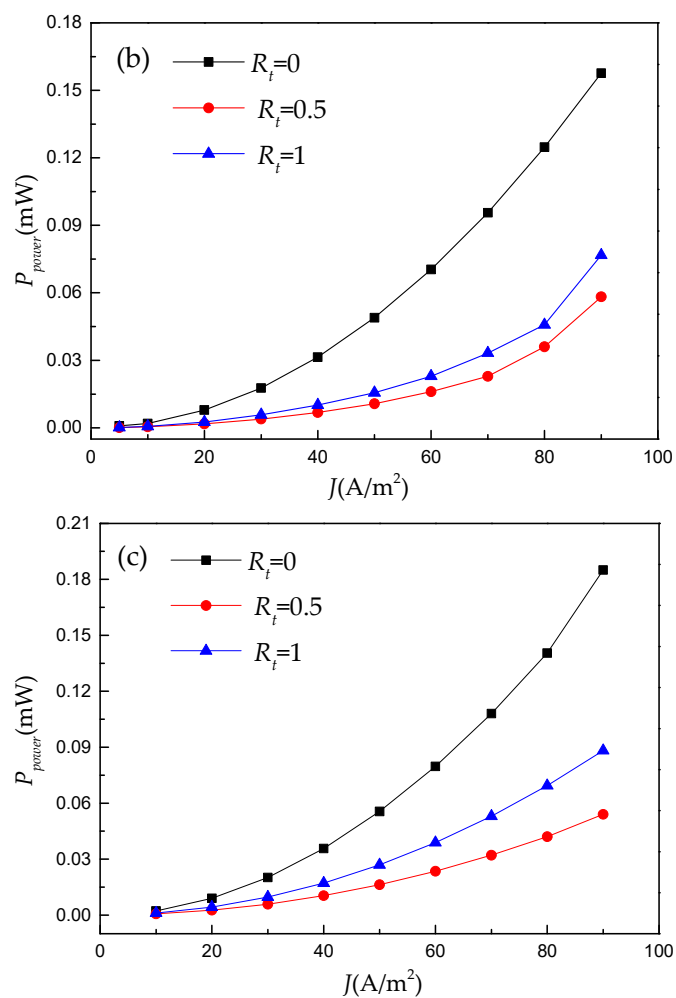
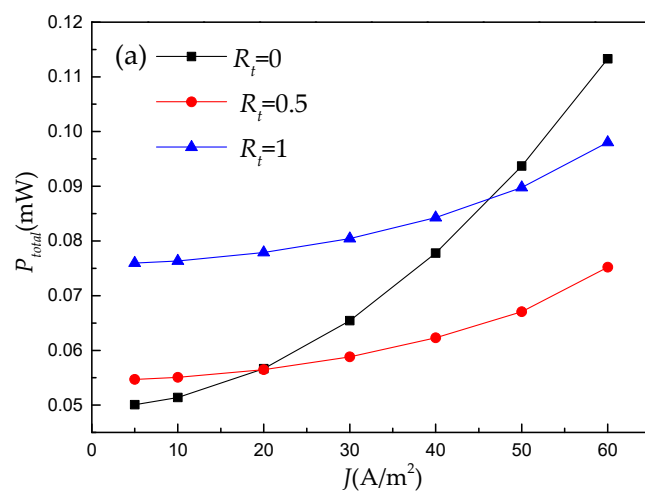


Figure 5. Cont.





**Figure 5.** Overpotential polarization loss with varying discharging current density and electrode architectures. (a)  $Q = 1$  mL/min, (b)  $Q = 2$  mL/min, (c)  $Q = 10$  mL/min.



**Figure 6.** Cont.

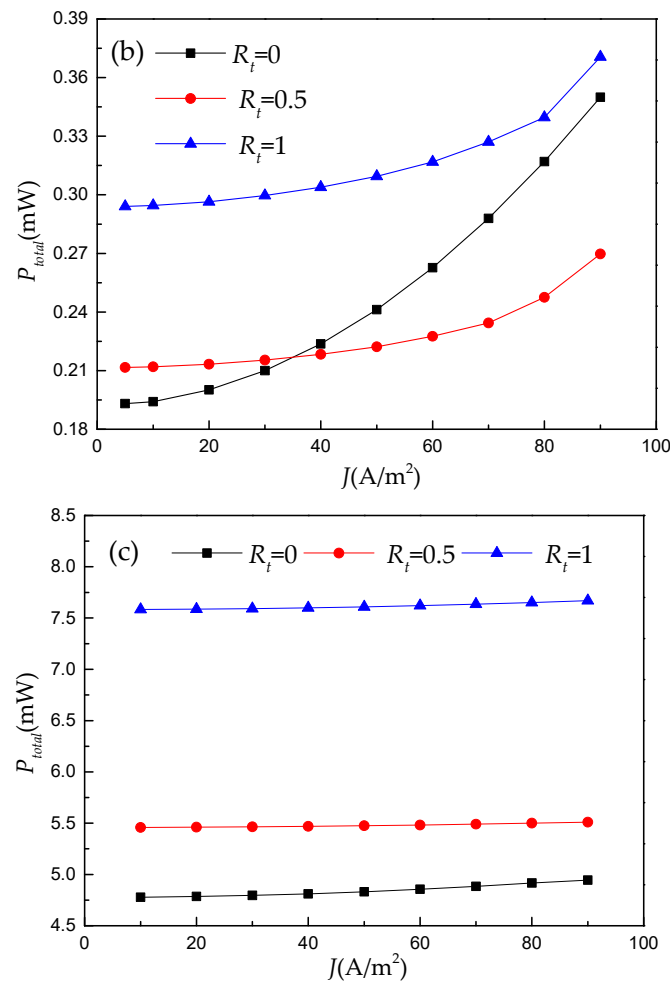


**Figure 6.** Total power loss with varying discharging current density and electrode architectures. (a)  $Q = 1$  mL/min, (b)  $Q = 2$  mL/min, (c)  $Q = 10$  mL/min.

### 3.2. RFB's Performance Prediction Using ANN Regression Model Coupled with GA

Although these above numerical cases can be compared to find the electrode architecture with the relatively low total power loss, the thickness ratio and operating conditions were selected within a limited number of discrete points due to the restrictions on computing resources. Consequently, based on the limited FEM simulation results, a suitable regression prediction model is also needed to approximate the functional relationship between RFB's performance and these impact factors. To predict the RFB's performance with a double-layer electrode, we established a multi-layer ANN model, which is integrated into the GA procedure to optimize the weight and threshold values of ANN. The population size and evolution iterations are key factors to impact the optimization quality. This paper defines the mean square error (MSE) between ANN's true value and predictive value to evaluate the training results' accuracy. As the population size is 160, the effect of evolution iterations on MSE is presented in Figure 7a. Since the genes with low predictive accuracy (i.e., fitness in this paper) are replaced constantly during the iterative evolution process, the predictive quality of ANN optimized by GA can be improved effectively after a sufficient iterative evolution. The predictive error can be significantly reduced with increasing evolution iterations. In the actual optimization process, we set the required predictive accuracy and the maximum iterations, thus promoting the reliability of ANN as far as possible. Moreover, we compared the predictive accuracy of ANN optimized by the different population sizes of GA. As shown in Figure 7b, the MSE of predictive results decreases as the GA with larger population size is applied to train ANN. As more genes are involved in the evolution process, GA has greater latitude in selecting the superior gene

with higher fitness. Consequently, as the population size has a fourfold increase, the MSE of predictive results falls by 33 times. To ensure training accuracy, a population size of 160 is employed in the following study of this paper. Figure 7c displays the regression training outcomes by comparing the predicted values with true values from the testing dataset. The predicted value in this figure is defined as  $P_{total}/Q$ . These outcomes predicted by ML are approximately in agreement with the actual values. Using the perfect prediction line to estimate the training effect, the determination coefficient ( $R^2$ ) can reach more than 0.999.

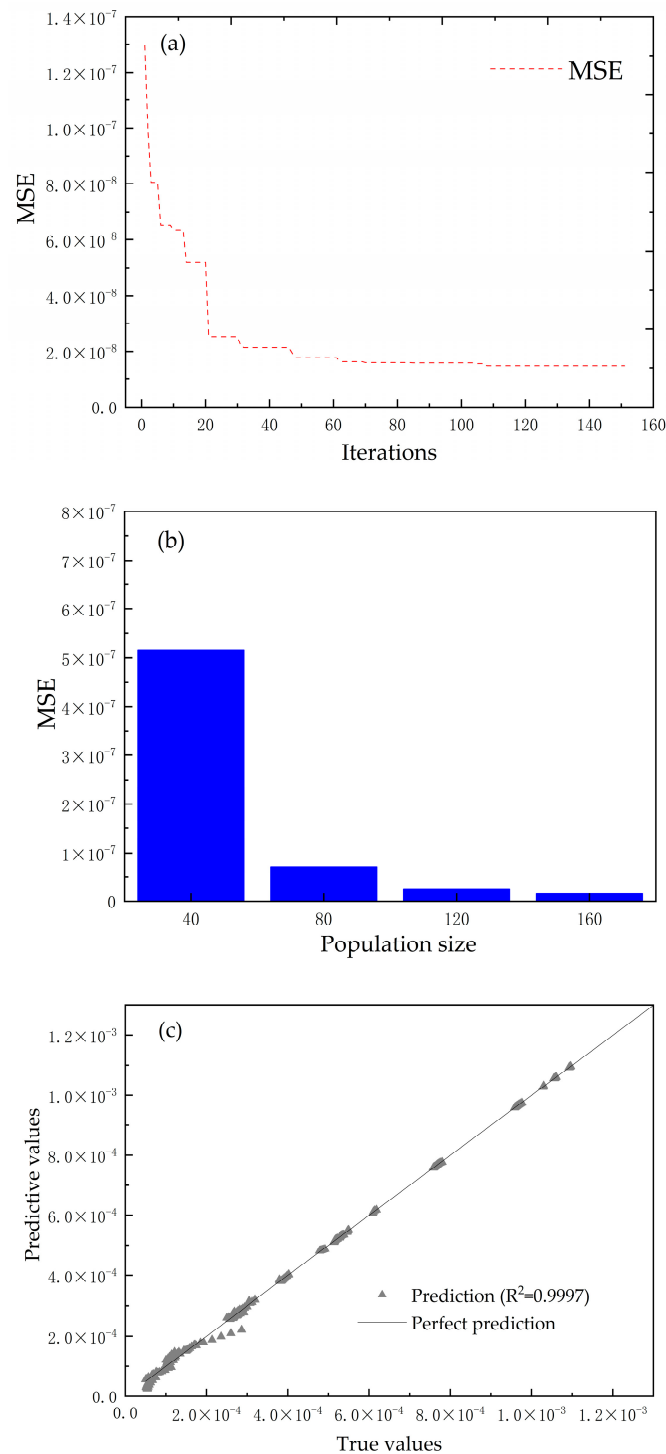


**Figure 7.** (a) Effect of evolution iterations on MSE, (b) Effect of population size on MSE, (c) Comparing predicted values with true values.

To compare the availability of this multi-layer ANN procedure coupled with GA, we introduced a series of popular ML regression models to train the identical training dataset. These models are divided into linear regression model (LM), support vector machine (SVM), ANN without GA, Gaussian process regression (GPR), and decision-making tree (DT). In particular, linear regression models include robust linearity, stepwise linearity and interaction effect linearity. Support vector machines include linear SVM, quadratic SVM and cubic SVM. Artificial neural networks include wide ANN, medium ANN and narrow ANN. Gaussian process regression models include square exponent GPR, quadratic rational GPR and matern 5/2 GPR. Decision-making tree models include rough DT, medium DT and fine DT. By testing the training effect, the MSEs of these ML regression models are calculated using the same testing set, and the comparative result is given in Figure 8. This result reveals that the accuracy of predictive values appears to be significantly different among these regression models. For different kinds of regression methods, GPR models have lower predictive errors; MSEs of three GPR models are all less than  $8 \times 10^{-8}$ . Nevertheless, the fine DT model has an MSE of  $1.59 \times 10^{-8}$ , which is the lowest predictive error within these popular regression models. It can be found that the multi-layer ANN coupled with GA can reach an MSE of  $1.54 \times 10^{-8}$ . This predictive error is significantly lower than other ANN without GA and is also lower than the error of fine DT. As a result, the proposed ML algorithm has good predictive accuracy compared with other ML regression models.

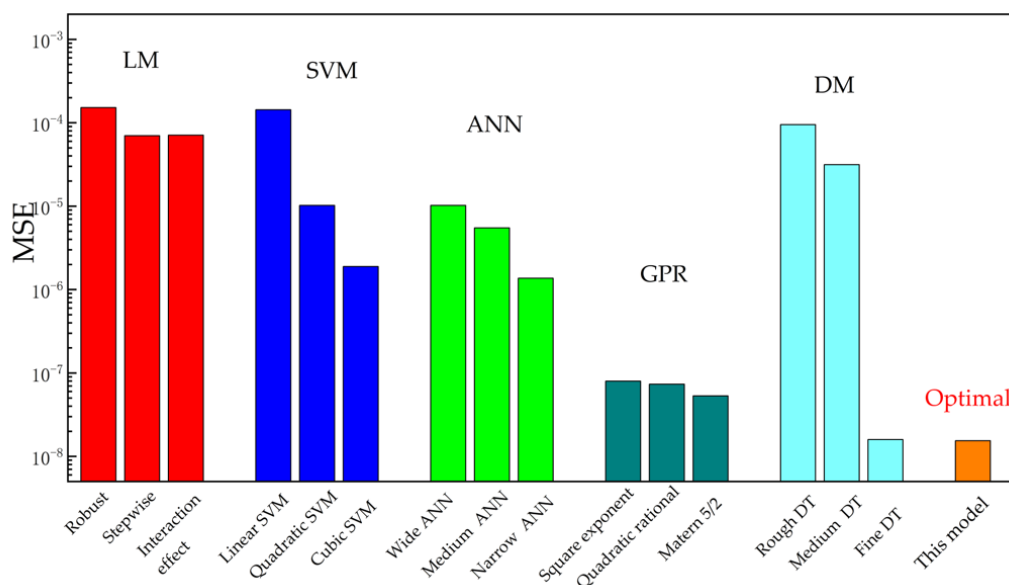
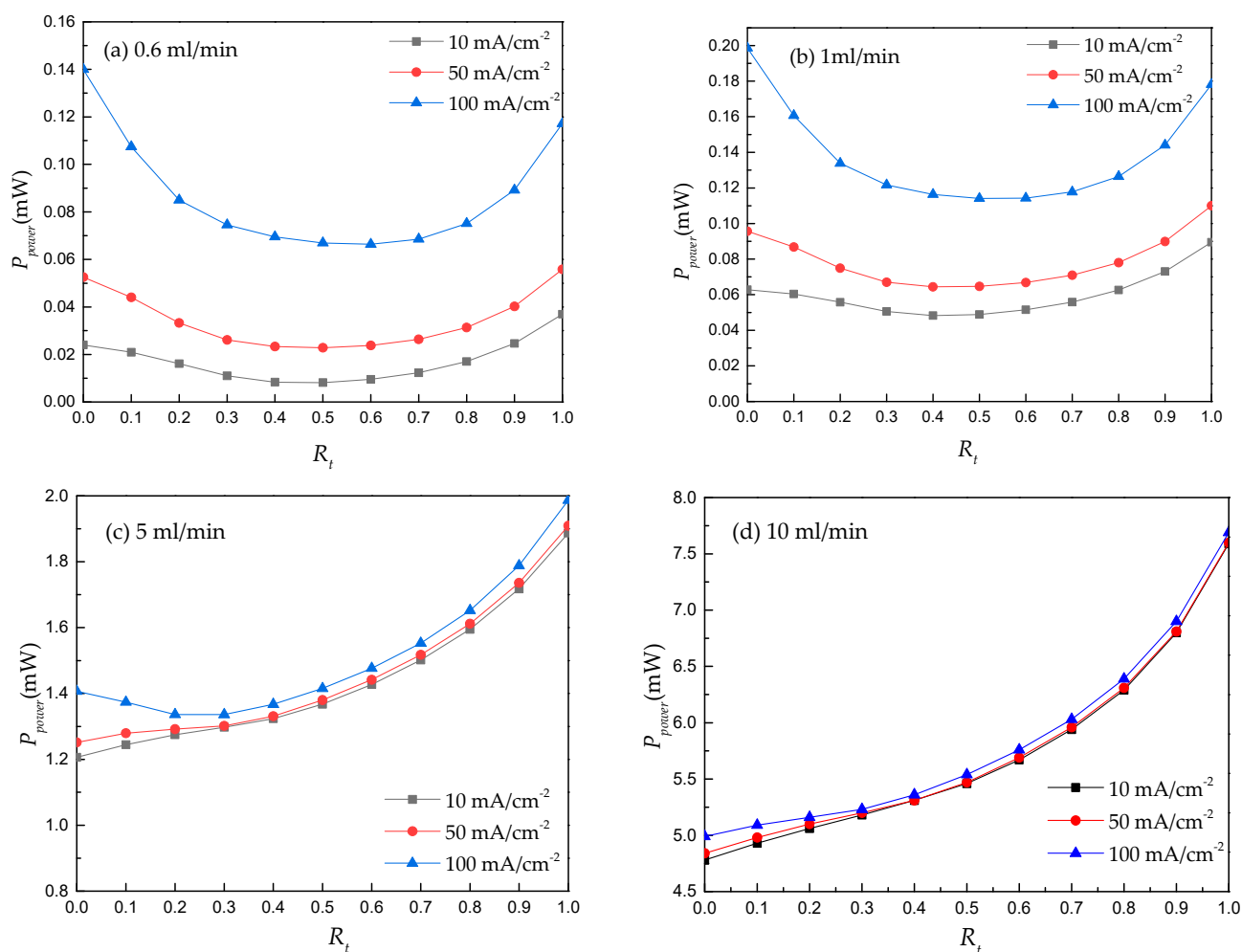


Figure 8. Training accuracy of different ML regression models.

One of the aims of the established ML regression model is to uncover the optimal thickness ratio of the double-layer electrode under the different operating conditions of a vanadium-iron RFB. Based on the well-trained regression model, the relationship between total power loss and the electrode's thickness ratio is predicted under different electrolyte flow rates and discharging current density, as shown in Figure 9. On the one hand, for the lower electrolyte flow rate (0.6 L/min and 1 L/min), the double-layer electrode architectures would achieve the optimum operational efficiency relative to CP and GF electrodes. On the other hand, under these low flow rate conditions, due to the electrochemical polarization resistance playing a main role in the operational power loss of the RFB, the composite electrode with gradient pore distribution makes a trade-off between electrolyte transfer resistance and electrochemical reaction resistance, thus improving the discharging performance of the vanadium-iron RFB as the current density varies from  $10 \text{ A/m}^2$  to  $100 \text{ A/m}^2$ . Furthermore, Figure 9a,b displays that the optimal thickness ratio of the double-layer electrode would be changed with different discharging current density conditions. As the electrolyte flow rate is 1 L/min, the optimal thickness ratio is 0.4 as

the current density is  $10 \text{ A/m}^2$ . However, at the higher current density, i.e.,  $100 \text{ A/m}^2$ , the 0.6 optimal thickness ratio achieves the minimum total power loss. The increasing discharging current density means a higher electrochemical reaction rate occurring on the surface of the carbon electrode. In that case, the higher proportion of the CP section can provide a larger specific surface area to reduce the charge transfer current density per unit area, thus alleviating the overpotential polarization loss at a higher discharging current density.



**Figure 9.** Predictive total power loss is affected by the electrode's thickness ratio. (a)  $Q = 0.6 \text{ mL/min}$ , (b)  $Q = 1 \text{ mL/min}$ , (c)  $Q = 5 \text{ mL/min}$ , (d)  $Q = 10 \text{ mL/min}$ .

On the other hand, because the electrolyte flow resistance increases rapidly with the increasing input flow rate, the pump power loss would dominate the total power loss of the RFB when the flow rate is higher than a critical value [26]. Under this flow rate condition, the electrode with higher porosity (i.e., mono-layer GF electrode) has a higher permeability, thus resulting in a low total power loss. Therefore, as shown in Figure 9c,d, the double-layer electrode architecture may not play a positive role in improving the RFB's performance as the electrolyte flow rate is larger than  $5 \text{ L/min}$ . If the electrolyte flow rate is  $5 \text{ L/min}$ , the total power loss of the double-layer electrode with  $R_t = 0.3$  is lower than that of the GF electrode ( $R_t = 0$ ) only under the highest discharging current density ( $100 \text{ A/m}^2$ ). Furthermore, if the electrolyte flow rate is  $10 \text{ L/min}$ , a GF electrode with low flow resistance is the best choice for minimizing the total power loss of a vanadium-iron RFB, compared with double-layer electrode architecture. As a result, although the RFB is unlikely to run in a fixed electrolyte flow rate and a fixed discharging/charging current

density, the pre-determined operating ranges (e.g.,  $Q$  and  $J$ ) are critical for designing the electrode architecture of an RFB.

In order to clarify the relationship between electrode architecture and operating ranges, Figure 10 summarizes the optimal thickness ratio of double-layer electrodes under the different electrolyte flow rates and current densities. Within the higher electrolyte flow rate and the lower discharging current density conditions (i.e., the black zone in Figure 10), the pump power loss is much higher than the polarization loss. Thus, the total power loss is governed by the flow resistance of the electrolyte passing through the porous electrode. Because this filtration resistance loss is inversely proportional to the porosity of porous media, the high-porosity GF electrode ( $R_t = 0$ ) is more suitable under these operating ranges compared with the CP electrode or double-layer electrode ( $R_t > 0$ ). On the contrary, the polarization loss is of the same magnitude as the pump power loss within the lower electrolyte flow rate and the higher discharging current density conditions (i.e., the color zone in Figure 10). Under these operating regions, the total power loss is affected synthetically by the electrolyte flow resistance and the electrochemical reaction resistance, thereby needing the double-layer electrode to achieve a trade-off between the pump power loss and the polarization loss. Hence, as shown in the color zone of Figure 10, if the CP electrode with an appropriate thickness ratio is assembled near the membrane side, the larger specific surface area provided by CP can effectively reduce the charge transfer resistance to decrease the polarization loss and the total power loss, compared with the mono-layer GF. Moreover, polarization loss would play a more prominent role in determining the total power loss with the decreasing flow rate and the increasing current density. This means a higher proportion of CP section is needed to obtain the optimal double-layer electrode architecture. In other words, the desired thickness ratio ( $R_t$ ) improves with the decreasing flow rate and the increasing current density, as shown in Figure 10. Furthermore, based on the known operating ranges of the RFB, the predictive results of the ML algorithm can aid in determining whether a double-layer electrode should be used in the vanadium-iron RFB and an appropriate thickness ratio of this double-layer electrode.

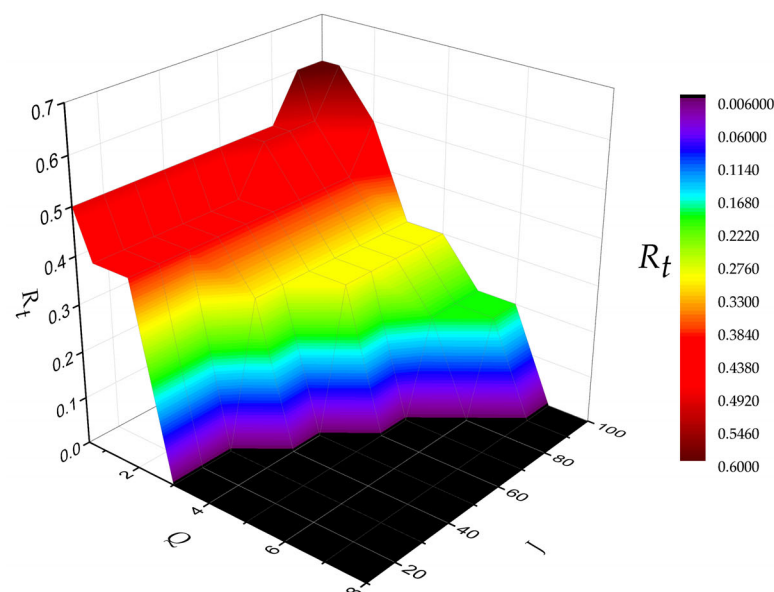


**Figure 10.** Optimal thickness ratio of double-layer electrode under different electrolyte flow rates and current densities. Note: The black zone means double-layer electrode architecture does not play a positive role in improving RFB's performance.

#### 4. Conclusions

Based on the finite-element numerical simulations of a single cell's galvanostatic discharging process to generate a training dataset, this work develops an ANN model

coupled with GA to aid the design of double-layer electrode architectures for a DES electrolyte-based vanadium-iron RFB. The main conclusions include the following:

- (1) The numerical results reveal that this double-layer electrode only plays a positive role under limited operating conditions. Hence, using an ML model to illustrate the regression relationship between RFB's performance and electrode architectures under different operating conditions is necessary.
- (2) The accuracy of this well-trained ML model is tested and compared with other popular regression models. The comparative result shows that the MSE of this multi-layer ANN coupled with GA can reach  $1.54 \times 10^{-8}$ . This predictive error is significantly lower than other ANNs without GA parameter optimization and is also lower than other popular ML regression models. The results show that the GA approach is one of the promising tools for training this multi-layer ANN. At the same time, intensive research should be conducted by comparing this optimization approach of GA with the commonly used optimizer, thus determining the applicable scope of this approach that has distinct advantages over other optimizers.
- (3) The performance prediction driven by this ML model shows that the pre-determined operating ranges (e.g.,  $Q$  and  $J$ ) are critical for designing the electrode architecture of an RFB. For example, based on the known operating ranges of the RFB, the predictive results of the ML algorithm can be used to estimate whether a double-layer electrode should be used in a non-aqueous vanadium-iron RFB and determine an optimal thickness ratio of this double-layer electrode.

Furthermore, this present work is conducted as a fixed total thickness of the electrode and the unchanged species transfer properties of the membrane. Therefore, a more comprehensive ML model should be established to consider further the effects of membrane materials and variational total electrode thicknesses on RFB's performance, which will expand the general applicability of ML prediction. Meanwhile, the role of ANN size on the training accuracy of this ML approach coupled with GA needs to be understood in further work.

**Author Contributions:** Conceptualization, methodology, writing—original draft preparation, Q.M.; validation, W.F.; formal analysis, J.X.; resources, Z.W.; supervision, Q.X. All authors have read and agreed to the published version of the manuscript.

**Funding:** This research was funded by the National Natural Science Foundation of China, grant number 52276066; and Science and Technology Research Project of Education Department of Jiangxi Province, grant number GJJ191111.

**Data Availability Statement:** Data will be made available on request.

**Acknowledgments:** This work is fully supported by the National Natural Science Foundation of China (No. 52276066) and Science and Technology Research Project of Education Department of Jiangxi Province (No. GJJ191111). We would also like to thank Prabhu Raj Balakrishnan for the helpful discussions.

**Conflicts of Interest:** The authors declare no conflict of interest.

## References

1. Li, M.; Case, J.; Minter, S.D. Bipolar Redox-Active Molecules in Non-Aqueous Organic Redox Flow Batteries: Status and Challenges. *ChemElectroChem* **2021**, *8*, 1215–1232. [[CrossRef](#)]
2. Cao, J.; Tian, J.; Xu, J.; Wang, Y. Organic Flow Batteries: Recent Progress and Perspectives. *Energy Fuels* **2020**, *34*, 13384–13411. [[CrossRef](#)]
3. Zhang, H.; Sun, C.; Ge, M. Review of the Research Status of Cost-Effective Zinc–Iron Redox Flow Batteries. *Batteries* **2022**, *8*, 202. [[CrossRef](#)]
4. Li, Z.; Jiang, T.; Ali, M.; Wu, C.; Chen, W. Recent Progress in Organic Species for Redox Flow Batteries. *Energy Storage Mater.* **2022**, *50*, 105–138. [[CrossRef](#)]
5. Chen, H.; Cong, G.; Lu, Y.C. Recent progress in organic redox flow batteries: Active materials, electrolytes and membranes. *J. Energy Chem.* **2018**, *27*, 1304–1325. [[CrossRef](#)]

6. Mushtaq, K.; Lagarteira, T.; Zaidi, A.A.; Mendes, A. In-situ crossover diagnostics to assess membrane efficacy for non-aqueous redox flow battery. *J. Energy Storage* **2021**, *40*, 102713. [[CrossRef](#)]
7. Cheng, R.; Xu, J.; Zhang, J.; Leung, P.; Ma, Q.; Su, H.; Yang, W.; Xu, Q. Facile segmented graphite felt electrode for iron-vanadium redox flow batteries with deep eutectic solvent (DES) electrolyte. *J. Power Sources* **2021**, *483*, 229200. [[CrossRef](#)]
8. Puttaswamy, R.; Mondal, C.; Mondal, D. An account on the deep eutectic solvents-based electrolytes for rechargeable batteries and supercapacitors. *Sustain. Mater. Technol.* **2022**, *33*, e00477. [[CrossRef](#)]
9. Liu, T.; Li, X.; Zhang, H.; Chen, J. Progress on the electrode materials towards vanadium flow batteries (VFBs) with improved power density. *J. Energy Chem.* **2018**, *27*, 1292–1303. [[CrossRef](#)]
10. Abbas, A.; Eng, X.E.; Ee, N.; Saleem, F.; Wu, D.; Chen, W.; Handayani, M.; A Tabish, T.; Wai, N.; Lim, T.M. Development of reduced graphene oxide from biowaste as an electrode material for vanadium redox flow battery. *J. Energy Storage*. **2021**, *41*, 102848. [[CrossRef](#)]
11. Lv, Y.; Han, C.; Zhu, Y.; Zhang, T.; Yao, S.; He, Z.; Dai, L.; Wang, L. Recent advances in metals and metal oxides as catalysts for vanadium redox flow battery: Properties, structures, and perspectives. *J. Mater. Sci. Technol.* **2021**, *75*, 96–109. [[CrossRef](#)]
12. Shi, Y.; Zhang, L.; Li, J.; Fu, Q.; Zhu, X.; Liao, Q.; Zhang, Y. 3-D printed gradient porous composite electrodes improve anodic current distribution and performance in thermally regenerative flow battery for low-grade waste heat recovery. *J. Power Sources* **2020**, *473*, 228525. [[CrossRef](#)]
13. Jing, M.; Zhang, C.; Qi, X.; Yang, Y.; Liu, J.; Fan, X.; Yan, C.; Fang, D. Gradient-microstructural porous graphene gelatum/flexible graphite plate integrated electrode for vanadium redox flow batteries. *Int. J. Hydrogen Energy* **2020**, *45*, 916–923. [[CrossRef](#)]
14. Chen, W.; Kang, J.; Shu, Q.; Zhang, Y. Analysis of storage capacity and energy conversion on the performance of gradient and double-layered porous electrode in all-vanadium redox flow batteries. *Energy* **2019**, *180*, 341–355. [[CrossRef](#)]
15. Jiang, H.R.; Zhang, B.W.; Sun, J.; Fan, X.; Shyy, W.; Zhao, T. A gradient porous electrode with balanced transport properties and active surface areas for vanadium redox flow batteries. *J. Power Sources* **2019**, *440*, 227159. [[CrossRef](#)]
16. Kim, Y.; Choi, Y.Y.; Yun, N.; Yang, M.; Jeon, Y.; Kim, K.J.; Choi, J.-I. Activity gradient carbon felt electrodes for vanadium redox flow batteries. *J. Power Sources* **2018**, *408*, 128–135. [[CrossRef](#)]
17. Wu, Q.; Lv, Y.; Lin, L.; Zhang, X.; Liu, Y.; Zhou, X. An improved thin-film electrode for vanadium redox flow batteries enabled by a dual layered structure. *J. Power Sources* **2019**, *410*, 152–161. [[CrossRef](#)]
18. Ma, Q.; Fu, W.; Zhao, L.; Chen, Z.; Su, H.; Xu, Q. A double-layer electrode for the negative side of deep eutectic solvent electrolyte-based vanadium-iron redox flow battery. *Energy* **2023**, *265*, 126291. [[CrossRef](#)]
19. Zhang, H.; Chen, N.; Sun, C.; Luo, X. Investigations on physicochemical properties and electrochemical performance of graphite felt and carbon felt for iron-chromium redox flow battery. *Int. J. Energy Res.* **2020**, *44*, 3839–3853. [[CrossRef](#)]
20. Takagishi, Y.; Yamanaka, T.; Yamaue, T. Machine Learning Approaches for Designing Mesoscale Structure of Li-Ion Battery Electrodes. *Batteries* **2019**, *5*, 54. [[CrossRef](#)]
21. Shodiev, A.; Duquesnoy, M.; Arcelus, O.; Chouchane, M.; Li, J.; Franco, A.A. Machine learning 3D-resolved prediction of electrolyte infiltration in battery porous electrodes. *J. Power Sources* **2021**, *511*, 230384. [[CrossRef](#)]
22. Wan, S.; Liang, X.; Jiang, H.; Sun, J.; Djilali, N.; Zhao, T. A coupled machine learning and genetic algorithm approach to the design of porous electrodes for redox flow batteries. *Appl. Energy* **2021**, *298*, 0306–2619. [[CrossRef](#)]
23. van Gorp, R.; van der Heijden, M.; Sadeghi, M.A.; Gostick, J.; Forner-Cuenca, A. Bottom-up design of porous electrodes by combining a genetic algorithm and a pore network model. *Chem. Eng. J.* **2022**, *455*, 139947. [[CrossRef](#)]
24. Ding, R.; Ding, Y.; Zhang, H.; Wang, R.; Xu, Z.; Liu, Y.; Yin, W.; Wang, J.; Li, J.; Liu, J. Applying machine learning to boost the development of high-performance membrane electrode assembly for proton exchange membrane fuel cells. *J. Mater. Chem.* **2021**, *9*, 6841–6850. [[CrossRef](#)]
25. Moses, I.A.; Joshi, R.P.; Ozdemir, B.; Kumar, N.; Eickholt, J.; Barone, V. Machine Learning Screening of Metal-Ion Battery Electrode Materials. *ACS Appl. Mater. Interfaces* **2021**, *13*, 53355–53362. [[CrossRef](#)]
26. Ma, Q.; Mao, C.W.; Zhao, L.J.; Chen, Z.; Su, H.; Xu, Q. A pore-scale study for reactive transport processes in double-layer gradient electrode as negative side of a deep eutectic solvent electrolyte-based vanadium-iron redox flow battery. *Electrochim. Acta* **2022**, *431*, 141110. [[CrossRef](#)]
27. Ma, Q.; Zhao, L.J.; Xu, J.C.; Su, H.; Zhang, W.; Yang, W.; Xu, Q. Pore-scale investigation of reactive transfer process in a deep eutectic solvent (DES) electrolyte-based vanadium-iron redox flow battery. *Electrochim. Acta* **2020**, *353*, 1364863. [[CrossRef](#)]
28. Ma, Q.; Xing, L.; Su, H.N.; Zhang, W.; Yang, W.; Xu, Q. Numerical investigation on the dispersion effect in vanadium redox flow battery. *Chem. Eng. J.* **2020**, *393*, 124753. [[CrossRef](#)]
29. Ma, Q.; Mao, C.W.; Fu, W.X.; Li, H.; Su, H.; Xu, Q. Numerical study of deep eutectic solvent electrolyte-based vanadium-iron redox flow battery with three-dimensional multi-layer porous electrode. *Int. J. Energy Res.* **2022**, *46*, 12820–12836. [[CrossRef](#)]
30. Mao, C.W.; Ma, Q.; Li, H.H.; Su, H.; Xu, Q. Numerical investigation of coupling effects of gradient porous electrode and flow channel pattern on iron-vanadium redox flow battery. *Int. J. Green Energy* **2022**, *19*, 1375–1387. [[CrossRef](#)]
31. Zhao, L.J.; Ma, Q.; Xu, Q.; Su, H.; Zhang, W. Performance improvement of nonaqueous iron-vanadium flow battery using chromium oxide-modified graphite felt electrode. *Ionics* **2021**, *27*, 4315–4325. [[CrossRef](#)]



32. Katoch, S.; Chauhan, S.S.; Kumar, V. A review on genetic algorithm: Past, present, and future. *Multimed. Tools Appl.* **2021**, *80*, 8091–8126. [[CrossRef](#)]
33. Sun, C.; Negro, E.; Nale, A. An efficient barrier toward vanadium crossover in redox flow batteries: The bilayer [Nafion/(WO<sub>3</sub>)<sub>x</sub>] hybrid inorganic-organic membrane. *Electrochim. Acta* **2021**, *378*, 138133. [[CrossRef](#)]

**Disclaimer/Publisher's Note:** The statements, opinions and data contained in all publications are solely those of the individual author(s) and contributor(s) and not of MDPI and/or the editor(s). MDPI and/or the editor(s) disclaim responsibility for any injury to people or property resulting from any ideas, methods, instructions or products referred to in the content.